

# 1 Antarctic Radio Frequency Albedo and Implications for Cosmic Ray Reconstruction

2 D. Z. Besson<sup>a</sup>, J. Stockham<sup>a</sup>, M. Sullivan<sup>a</sup>, P. Allison<sup>b,e</sup>, S. W. Barwick<sup>d</sup>, B. M. Baughman<sup>e</sup>, J. J. Beatty<sup>e</sup>, K. Belov<sup>c</sup>, S. Bevan<sup>f</sup>,  
 3 W. R. Binns<sup>g</sup>, C. Chen<sup>h</sup>, P. Chen<sup>h</sup>, J. M. Clem<sup>i</sup>, A. Connolly<sup>e</sup>, D. De Marco<sup>i</sup>, P. F. Dowkont<sup>g</sup>, M. DuVernois<sup>b</sup>, D. Goldstein<sup>d</sup>, P.  
 4 W. Gorham<sup>b</sup>, E. W. Grashorn<sup>e</sup>, B. Hill<sup>b</sup>, S. Hoover<sup>c,k,l</sup>, M. Huang<sup>j</sup>, M. H. Israel<sup>g</sup>, A. Javaid<sup>i</sup>, J. Kowalski<sup>b</sup>, J. Learned<sup>b</sup>, K. M.  
 5 Liewer<sup>i</sup>, S. Matsuno<sup>b</sup>, B. C. Mercurio<sup>e</sup>, C. Miki<sup>b</sup>, M. Mottram<sup>f</sup>, J. Nam<sup>d,h</sup>, C. J. Naudet<sup>i</sup>, R. J. Nichol<sup>f</sup>, K. Palladino<sup>e</sup>, A.  
 6 Romero-Wolf<sup>b,j</sup>, L. Ruckman<sup>b</sup>, D. Saltzberg<sup>c</sup>, D. Seckel<sup>i</sup>, R. Y. Shang<sup>h</sup>, M. Stockham<sup>a</sup>, G. S. Varner<sup>b</sup>, A. G. Vieregg<sup>c,m</sup>, and Y.  
 7 Wang<sup>h</sup>

8 <sup>a</sup>Department of Physics and Astronomy, University of Kansas, Lawrence, Kansas 66045, USA

9 <sup>b</sup>Dept. of Physics and Astronomy, University of Hawaii at Manoa, Honolulu, HI 96822.

10 <sup>c</sup>Dept. of Physics and Astronomy, University of California, Los Angeles, CA 90095.

11 <sup>d</sup>Department of Physics, University of California, Irvine, California 92697, USA

12 <sup>e</sup>Department of Physics, Ohio State University, Columbus, Ohio 43210, USA

13 <sup>f</sup>Department of Physics and Astronomy, University College London, London, United Kingdom

14 <sup>g</sup>Department of Physics, Washington University in St. Louis, Missouri 63130, USA

15 <sup>h</sup>Department of Physics, National Taiwan University, Taipei, Taiwan 10617

16 <sup>i</sup>Department of Physics, University of Delaware, Newark, Delaware 19716, USA

17 <sup>j</sup>Jet Propulsion Laboratory, Pasadena, California 91109, USA

18 <sup>k</sup>Kavli Institute for Cosmological Physics, University of Chicago, 5640 South Ellis Avenue, Chicago, IL 60637

19 <sup>l</sup>Enrico Fermi Institute, University of Chicago, 5640 South Ellis Avenue, Chicago, IL 60637

20 <sup>m</sup>Harvard-Smithsonian Center for Astrophysics, Cambridge, Massachusetts 02138, USA

## 21 Abstract

22 From an elevation of  $\sim 38$  km, the balloon-borne ANtarctic Impulsive Transient Antenna (ANITA) is designed to detect the up-  
 23 coming radio frequency (RF) signal resulting from a sub-surface neutrino-nucleon collision. Although no neutrinos have been  
 24 discovered thus far, ANITA is nevertheless the only experiment to self-trigger on radio frequency emissions from cosmic-ray  
 25 induced atmospheric air showers. In the majority of those cases, down-coming RF signals are observed via their reflection from  
 26 the Antarctic ice sheet and back up to the ANITA interferometer. Estimating the energy scale of the incident cosmic rays therefore  
 27 requires an estimate of the fractional power reflected at the air-ice interface. Similarly, inferring the energy of neutrinos interacting  
 28 in-ice from observations of the upwards-directed signal refracting out to ANITA also requires consideration of signal coherence  
 29 across the interface. By comparing the direct Solar RF signal intensity measured with ANITA to the surface-reflected Solar signal  
 30 intensity, as a function of incident elevation angle relative to the surface  $\theta_i$ , we estimate the power reflection coefficients  $\mathcal{R}(\theta_i)$ .  
 31 We find general consistency between our average measurements and the values of  $\mathcal{R}(\theta_i)$  expected from the Fresnel equations[1],  
 32 separately for horizontal- vs. vertical-polarizations (“HPol” and “VPol”, respectively).

33 **Keywords:** radioglaciology, interferometry, cosmic rays

## 34 1. Introduction

### 35 1.1. The ANITA Experiment

36 Initiated in 2003, the Antarctic Impulsive Transient Antenna (ANITA) is a balloon-borne antenna array primarily designed to  
 37 detect radio wave pulses caused by neutrino collisions with ice[2]. The basic instrument consists of a suite of 40 quad-ridged  
 38 horn antennas, optimized over the frequency range 200-1200 MHz, with separate outputs for vertically vs. horizontally-polarized  
 39 incident radio frequency signals, mounted to a high-altitude balloon. From an elevation of  $\sim 38$  km, the payload observes the  
 40 Antarctic continent in a circumpolar trajectory. Two one-month long missions (ANITA-I; Dec. 2006-Jan. 2007 and ANITA-II;  
 41 Dec. 2008-Jan. 2009) have yielded world’s-best limits to the flux of Ultra-High Energy (“UHE”, corresponding to energies in  
 42 excess of  $10^{19}$  eV) neutrinos in the energy range to which ANITA is sensitive[4, 5]. Nevertheless, model-dependent calculations  
 43 of surface effects show considerable variation in the fraction of signal power emerging from within the dense ice target medium  
 44 and across the interface to the receiver; this is also true for experiments seeking to measure neutrino interactions within the lunar  
 45 regolith[6, 7, 8, 9]. An interferometric analysis of the ANITA-I data sample provided a statistically large (16 events) sample  
 46 of radio frequency signals attributed to the geomagnetic + Askaryan radiation associated with cosmic-ray induced extensive air  
 47 showers[12] (EAS); those events marked the first self-triggered detection of EAS via their radio emissions.

48 The analysis described below is based on ANITA-II data. After launching from McMurdo Station in December, 2008, ANITA-  
 49 II was aloft for a period of 31 days with a typical instantaneous duty cycle exceeding 95%. Although the external experimental  
 50 conditions (livetime and flight path) were more favorable for ANITA-II than for ANITA-I, the sample of detected extensive air  
 51 shower (EAS) events was somewhat smaller for ANITA-II, primarily owing to a modification to the trigger that favored neutrino  
 52 detection, but, as realized *ex post facto*, dis-favored EAS detection[10]. The ANITA-III launch, scheduled for December, 2013,  
 53 is expected to result in an improvement by a factor of  $\sim 100$  in the number of detected air shower events relative to ANITA-I.  
 54 Correspondingly, we have sought to determine the surface reflectivity in advance of that upcoming ANITA-III mission.

55 **1.2. ANITA Data Acquisition and Signal Reception Chain**

56 The ANITA detector is designed to efficiently collect radio signal over a 1 GHz bandwidth, with electronics and trigger config-  
 57 ured to produce the minimum possible energy threshold. The front-end Seavey quad-ridge antennas provide the first element in  
 58 the ANITA radio wave signal processing chain. These horn antennas have separate VPol vs. HPol signal polarization readouts,  
 59 and each has a field-of-view of approximately 25° half-width-half-maximum (FWHM) in both azimuth angle ( $\phi$ ) and zenith angle  
 60 ( $\theta$ ). Following the Seavey antennas, high- and low-pass filtering restricts the system bandpass to 200–1200 MHz, after which  
 61 signals are split into a ‘trigger’ path consisting of a heirarchy of trigger conditions (“levels”) and a ‘digitization’ path. If all levels  
 62 of the three-tiered, heirarchical trigger are satisfied, the digitized signals, consisting of 256 voltages sampled for each antenna at  
 63 2.6 GSa/s, are then stored to disk. During typical ANITA-II data-taking conditions, data were written at a rate of approximately  
 64 10 Hz. The overwhelming majority of these triggers are due to upward excursions of the thermal radio photosphere.

65 **1.3. ANITA interferometry**

66 Beginning with the eighty 100-ns duration voltage waveforms which are taken during an ANITA event trigger (40 antennas  $\times$  2  
 67 polarizations per antenna), familiar radio interferometry techniques are used to identify localized radio sources. To determine the  
 68 direction of an external impulsive source, the full solid angle is first divided into an  $N_\theta \times N_\phi$  grid (typically, 180  $\times$  360) in elevation  
 69 and azimuth, respectively. Next, an inter-channel cross-correlation sum is calculated for each point in the grid, by shifting cross-  
 70 correlated waveforms by the relative propagation time delays that would be incurred, channel-by-channel, for a putative source at  
 71 that  $(\theta, \phi)$  grid point. Formally, the cross-correlation  $C$ , for two channels  $i$  and  $j$  can be written as the dot product of the voltage time  
 72 series for channel  $i$   $V_i(t)$  and the voltage time series for channel  $j$   $V_j(t)$ , shifted by the calculated time delay  $\delta t_{ij}^S(\theta, \phi)$  corresponding  
 73 to the putative source  $S$  at  $(\theta, \phi)$ , for the  $N$  samples in the dot product (equal to the number of samples in the waveform minus the  
 74 number of time samples corresponding to the time shift  $\delta t_{ij}$ ). To minimize sensitivity to channel-dependent gain variations, this  
 75 cross-correlation coefficient is normalized relative to the rms voltages in the two channels  $\sigma(V_i)$  and  $\sigma(V_j)$ :

$$c_{ij} = \sum_{n=1}^N V_i^S(t_n) V_j^S(t_n + \delta t_{ij}^S) / \sqrt{\sigma(V_i)\sigma(V_j)} \quad (1)$$

76 In the limit of a strong source which dominates the 100-ns waveform, the cross-correlation rises linearly with signal voltage  $V^S$ ,  
 77 since  $\sigma(V) \sim V^S$ . In the limit of a very weak source,  $\sigma(V)$  is largely independent of  $V^S$  and the cross-correlation increases  
 78 quadratically with signal voltage. The high signal-to-noise (SNR) events that comprise the ANITA EAS sample correspond to the  
 79 former case. The Solar signal described below corresponds to the latter case, and therefore, in the case of signals from the Sun,  
 80 the cross-correlation coefficient scales with the radio power received. The total cross-correlation  $C$  is calculated by summing over  
 81 all independent  $(i, j)$  pairs. The polar and azimuthal angles of a putative source are then assigned to that grid pixel giving the  
 82 highest total cross-correlation  $C$ . More extensive details on the construction of the ANITA interferometric map can be found in  
 83 the literature[11].

84 An obvious design goal of ANITA is to localize sources with the best-possible pointing resolution. Unlike source vertexing  
 85 algorithms using hit-time assignments from threshold-crossings, interferometry is particularly suited for continuous-wave (CW)  
 86 sources. As illustrated by Monte Carlo simulations (Fig. 1), the interferometric reconstruction resolution improves, roughly  
 87 linearly, with the frequency of the source. Alternately, the angular size of the interferometric image provides information on the  
 88 source frequency content, with wider images implying power spectra weighted preferentially to lower frequencies.

89 A discone transmitter, buried approximately 100 m into the ice sheet at a remote site near Taylor Dome, has been used to assess  
 90 the interferometric source reconstruction resolution for signals with broad frequency content. For that transmitter, we obtain values  
 91 of 0.25 degrees in elevation and 0.56 degrees in azimuth for the ANITA-II flight. For comparison, the intrinsic Solar radio source  
 92 size is of order 1 degree in the sky.

93 **1.4. ANITA Radio Air Shower Observations**

94 A maximum likelihood analysis of the 16 ANITA-I EAS detections implied a mean energy of  $1.5 \pm 0.4(\text{stat})^{+2.0}_{-0.3}(\text{sys}) \times 10^{19}$   
 95 eV for the cosmic ray primary[12], with the highest primary estimated at an energy approximately equal to the GZK-scale[13]  
 96 of  $\sim 6 \times 10^{19}$  eV. Agreement in the spectral characteristics between the two cosmic rays incident in the six degree elevation  
 97 range between payload horizontal  $\theta^P=0$  and the Earth’s horizon at  $\theta^P = -6^\circ$ , compared to the 14 cosmic rays observed via their  
 98 reflections, indicate that surface roughness effects are not large, albeit with very limited statistics. That sample was supplemented  
 99 with an additional four reflected events observed with ANITA-II. Interestingly, two of the ANITA-II events featured reflection  
 100 points consistent with sea ice, for which the dielectric contrast relative to the air, and therefore the fractional reflected power, is  
 101 expected to be larger compared to reflections from sheet ice. Using the coordinate convention to be followed later in this paper for  
 102 comparing intensity measurements to expectations from the Fresnel equations, with the signal angle of incidence  $\theta_i$  defined relative  
 103 to a tangent on the surface, the incidence angles for the ANITA radio-reflected EAS sample is shown in Figure 2. From simple  
 104 solid angle considerations ( $d\Omega \sim \cos \theta d\theta$ ), we expect the acceptance to decrease with elevation angle. Additionally, since the  
 105 antennas are canted at -10 degrees relative to the payload horizontal, large values of  $\theta$  are increasingly experimentally suppressed.  
 106 Correspondingly, the observed EAS sample is primarily detected in the angular range  $\theta \lesssim 25$  degrees.

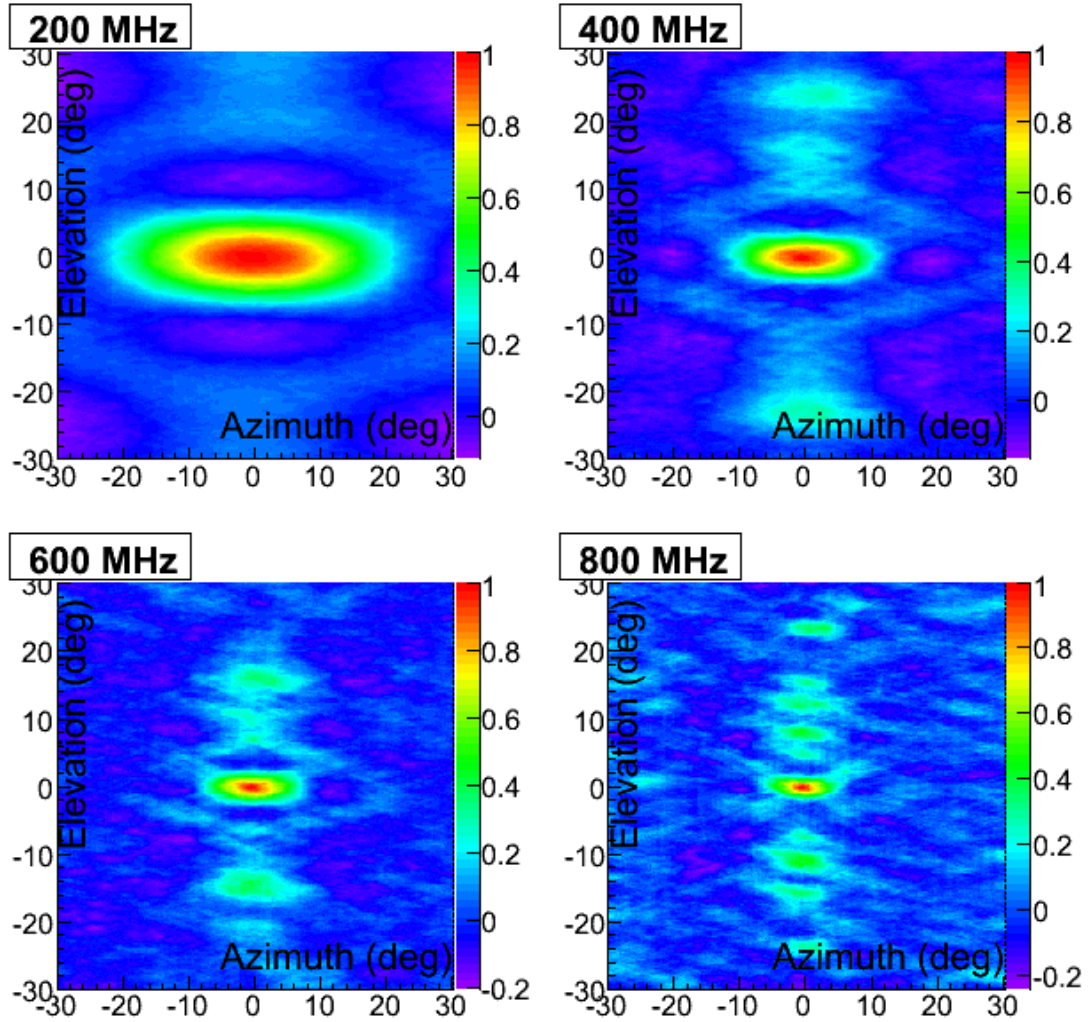


Figure 1: Interferometric map for simulated 200, 400, 600, and 800 MHz continuous-wave source at  $(\theta_S^P, \phi_S = 0, 0)$ .

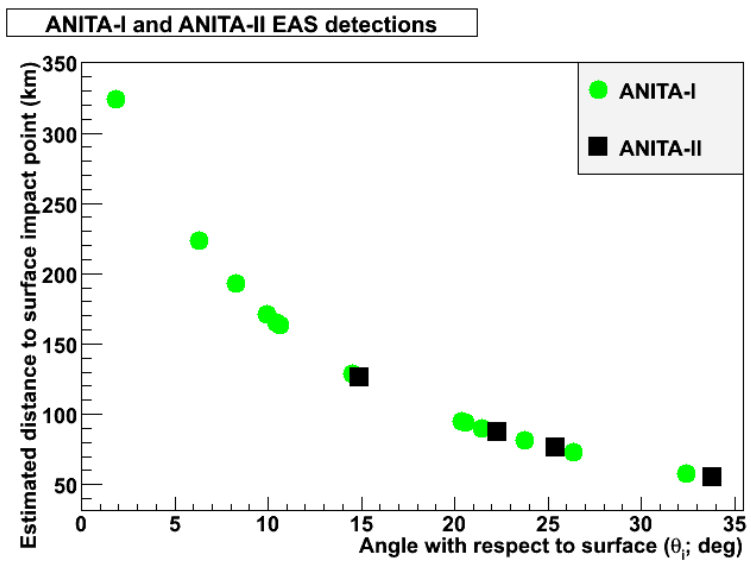


Figure 2: Elevation angle  $\theta_i$ , relative to the horizon, for the 14 ANITA-I, and 4 ANITA-II cosmic ray events observed via their radio emissions. Indicated distances are estimated.

## 107 2. Surface Roughness, General Considerations

108 According to the Rayleigh criterion, the magnitude of variation in surface height  $h$ , as measured along the line of the incoming  
109 radar must satisfy the condition  $h \cos(\phi) < 0.125$  ( $\phi_L$  here denotes the “look angle”) for the surface to be considered ‘smooth’.  
110 In the limit of perfect smoothness ( $h \rightarrow 0$ , corresponding to “specular reflection”), the Fresnel equations prescribe the fractional  
111 reflected signal intensity, as a function of incidence angle  $\theta_i$ . Deviations from smoothness result in a  $\theta_i$ -dependent redistribution  
112 of the reflected signal power. Depending on the geometry of the surface features, the wavelength, and the dielectric contrast  
113 across a surface, surface roughness can translate into either an enhancement, or reduction in the magnitude of reflected power, and  
114 correspondingly an anti-correlated reduction or enhancement in the amount of power transmitted across the surface.

## 115 3. Antarctic Surface Reflectivity

### 116 3.1. Visible Frequencies

117 The polar albedo is one of the crucial inputs to climate models, given its importance in determining the thermal equilibrium  
118 between Earth and Sun. Since the Solar power spectrum peaks in the visible, measurements of Solar reflectivity have typically  
119 focused on the 3900-6600 Å regime[14]. At such scales, sastrugi effects dominate, as a function of look angle  $\phi_L$  relative to the  
120 sastrugi alignment. Long-term studies (particularly at South Pole Station) have established periodic variations in the Solar albedo  
121 in the visible wavelength interval, over  $\sim 5$  year time scales[15]. Such measurements can also be used as a proxy for wind direction  
122 measurements[16], to the extent that albedo observations probe wind-blown sastrugi orientation.

### 123 3.2. Prior Measurements at Lower Frequencies

124 The Earth has, to date, been extensively mapped in the Ku-band (12-18 GHz)[17, 18] and also in the lower-frequency C-  
125 band (2-4 GHz), most recently, and most comprehensively by the Canadian-based RADARSAT satellites. These relatively high  
126 frequencies, and correspondingly small wavelengths compared to the typical scale of surface features probe not only pure ‘surface’  
127 features, but also sub-surface volumetric scattering due to, e.g., buried sastrugi. The absolute/relative RADARSAT signal return  
128 strength calibration of 2 dB/(1 dB) is sufficient to map the backscattering power across the Antarctic continent (Fig. 3), which  
129 exhibits variations of order 20 dB. Those results are qualitatively consistent with the Envisat satellite Ku-band backscatter[19],  
130 albeit with some large deviations, particularly around the Ross Ice Shelf.

131 The Envisat C-band backscattering results generally follow the trend shown in Figure 4, but with the C-band backscattering  
132 strength over West Antarctica reduced by  $\sim 2$ -5 dB; the backscattering signal in East Antarctica is in general agreement with the  
133 Ku-band scattering to within 2-3 dB.

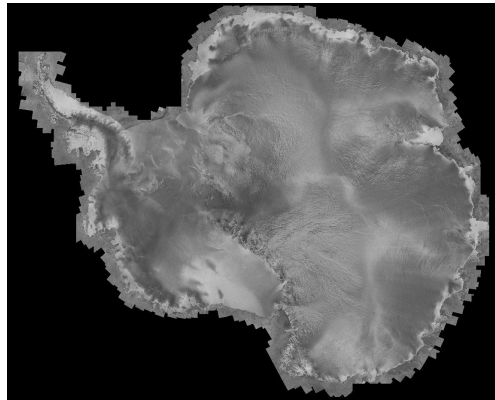


Figure 3: RADARSAT Ku-band backscattering coefficient  $\sigma_0$ . Maximum contrast corresponds to a variation of almost 20 dB in measured reflected power[17]. No corrections have been made for look angle effects.

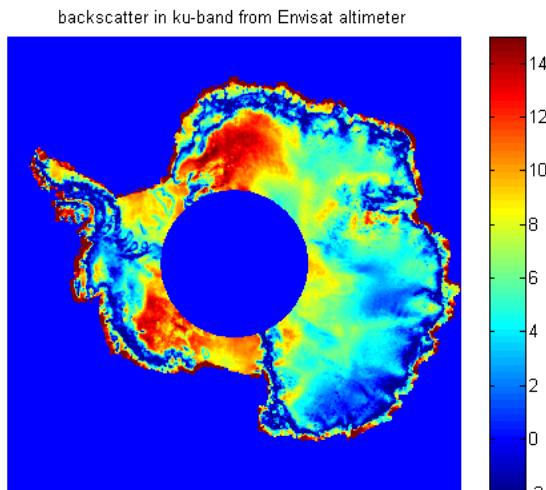
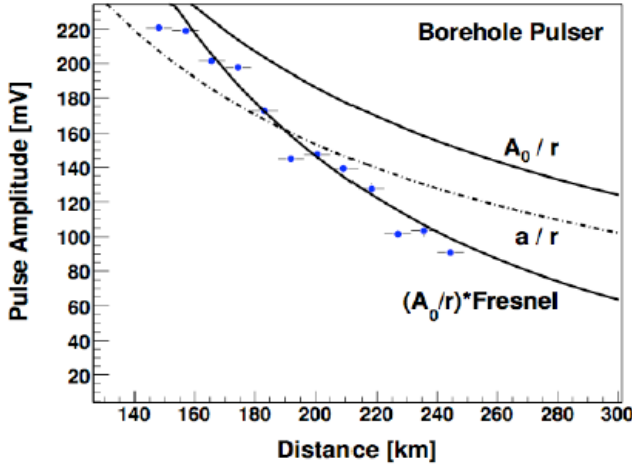


Figure 4: Envisat Ku-band backscattering coefficient[19], in units of dB. No corrections have been made for look angle effects.

133 Comparable data are not readily available at the higher frequencies of interest to the ANITA mission, although the precision  
134 of three-dimensional satellite maps of the entire Antarctic continent, such as those provided by LandSat, is now approaching  
135 dekameter scales. Proposals are now under consideration to convert photographic images collected during traverses of the Antarctic  
136 interior into surface roughness maps, although those would also sample only a very limited fraction of the Antarctic terrain.

137 Using the dedicated Taylor Dome discone transmitter, a previous ANITA-I study found reasonable agreement between the  
138 measured radio frequency signal strength at the gondola and the expectation from Snell’s Law, knowing the relative geometry of  
139 ANITA-I and the Taylor Dome calibration pulser (Figure 5), albeit over a very limited angular range. That study indicates that



2

Figure 5: Measured ANITA-I calibration pulser received signal voltage (data points), compared to signal voltages without inclusion of Fresnel factors (labeled “ $a/r$ ” and “ $A_0/r$ ”), and with inclusion of estimated Fresnel transmission coefficient across ice-air interface  $((A_0/r)*\text{Fresnel})$ .

141 surface roughness effects within that range, and in that portion of the continent, are not large. A direct measurement of surface  
 142 height variation[2] at the Taylor Dome calibration pulser site, as well as studies of local radio-frequency propagation through the  
 143 surface[3], also implied only modest surface roughness RF effects, for that one geographically limited site.

#### 144 4. Interferometry Applied to Solar Imaging

145 Absent bursts or flares, the Sun conveniently provides the ANITA mission an uninterrupted, unpolarized, (relatively) constant  
 146 power calibration source. However, since the Solar emissions in the ANITA bandpass are typically sub-threshold relative to the  
 147 ANITA trigger requirements, the Solar image is only clearly visible after adding many interferometric images in an heliocentric  
 148 coordinate system. For our current analysis, we add  $\sim 10^3 - 10^4$  events, excluding triggers containing high signal-to-noise sources  
 149 to elucidate the Solar signal.

150 To illustrate the expected signals, Figures 6 and 7 show simulated interferometric maps, for which a single point source, with  
 151 a flat frequency spectrum, has been modeled at the indicated elevation angle. Although reflection effects are absent from these  
 152 maps, we nevertheless observe some fringing characteristic of ANITA interferograms, and resulting from regular lateral or vertical  
 153 spacing of the ANITA horn receiver antennas. We note that for a source at a payload elevation  $\theta_S^P$ , fringing tends to produce  
 154 an enhancement at an elevation angle typically a few degrees below  $-\theta_S^P$  and therefore contributes some contamination to our  
 155 measured reflection power, with a magnitude that grows with  $\theta_S^P$ , requiring a small correction to our raw, extracted reflection  
 156 signals.

157 Fig. 8 shows the image of the Sun both in vertical and horizontal polarizations in data, after co-adding 10000 events, acquired  
 158 over a time of approximately 20 minutes. During that time, the Sun typically moves 0.5 degrees in the sky. As the Sun has no  
 159 intrinsic polarization, we expect approximately equal source intensities in each polarization, consistent with observation. We note  
 160 the presence of fringe effects in the interferometric map; such background effects are additionally complicated by the celestial  
 161 proximity of the galactic center to the Sun itself. Over the course of the ANITA-II flight, Sagittarius A\* is approximately 5 degrees  
 162 higher in elevation relative to the Sun, and within 25 degrees in azimuth, crossing the Solar azimuth roughly midway into the  
 163 flight.

##### 164 4.1. Cross-check of measurement procedure

165 We have conducted cross-checks to verify the numerical veracity of the interferometric technique, as applied to the Sun, as  
 166 follows.

###### 167 4.1.1. Variation of Solar signal strength with time

168 For a stationary summer observer at latitudes below the Antarctic circle, the Sun is expected to trace a sinusoid across the sky  
 169 over a diurnal period. We observe an obvious 24-hour cycle of Solar source intensity (Figure 9), as tracked for an 8-day period of  
 170 the flight following the balloon’s launch from McMurdo Station.

###### 171 4.1.2. Antenna Gain vs. Elevation

172 Over the course of a typical one-month Dec.-Jan. Long-Duration Balloon (LDB) Antarctic mission, the Sun’s elevation in the  
 173 sky, relative to the payload “horizontal”  $\theta_{\text{payload}}$ , varies between 10 and 40 degrees, and therefore allows an in-flight determination  
 174 of the polar beam pattern for the ANITA dual-polarization quad-ridged horn antennas. Figure 10 overlays the dependence of the  
 175 peak interferometric Solar power (defined as the magnitude of the highest-amplitude pixel in the Solar interferometric map) on

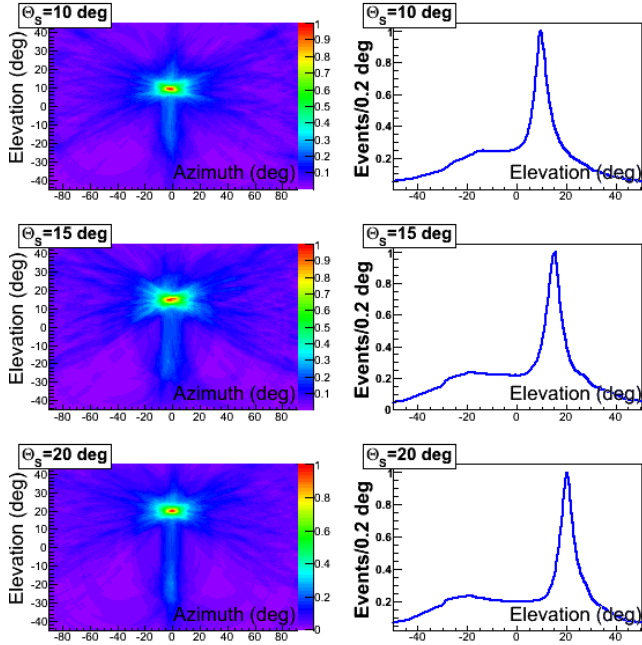


Figure 6: Interferometric map for simulated source at 10, 15, and 20 degree payload elevations, and projections onto elevation axis (right). Color scale has units of  $(Voltage)^2$ .

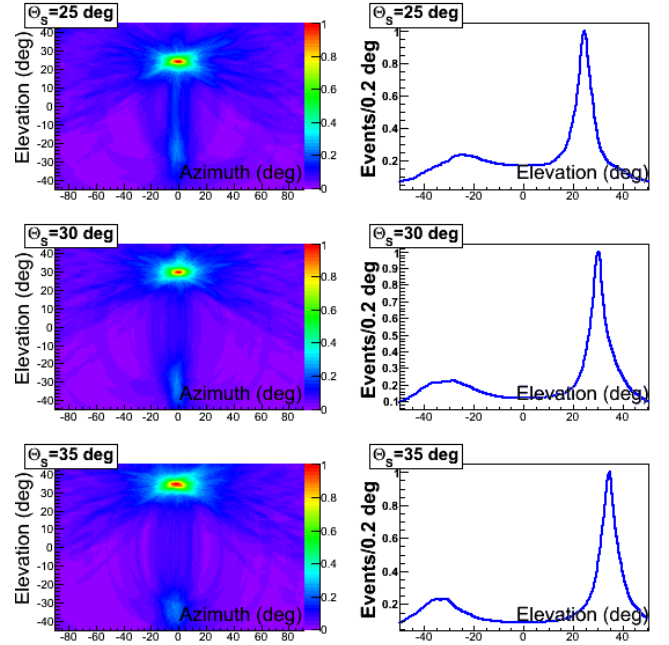


Figure 7: Interferometric map for simulated source at 25, 30, and 35 degree payload elevations (left), and projections onto elevation axis (right). Color scale has units of  $(Voltage)^2$ .

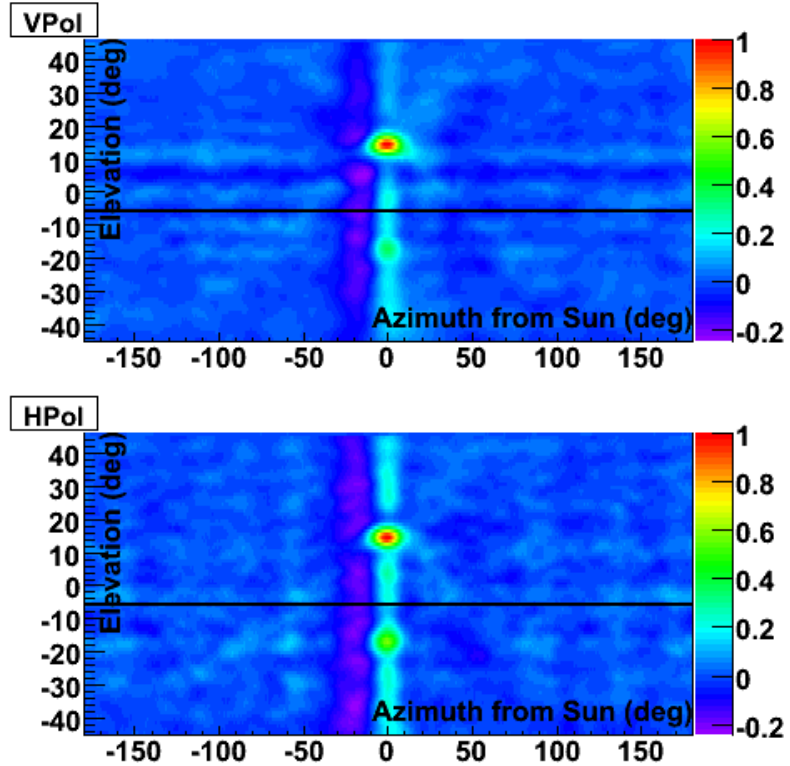


Figure 8: Interferograms (top, VPol and bottom, HPol) formed by tracking the location of the Sun for 10000 events. Normalization is identical for both top and bottom plots. For this plot, we use payload coordinates, for which the horizontal plane is defined as  $0^\circ$ , with elevation angles towards the zenith/(nadir) defined as positive/negative). Interferograms are stacked to account for both the motion of the Sun, as well as the translational motion of the ANITA gondola across the Earth's surface and the rotational motions of ANITA relative to its vertical and horizontal axes. Horizontal fringes more evident in VPol are consistent with effects due to the warm/cold ice/air discontinuity at the horizon, indicated by solid black line at  $\theta^P = -6$  degrees.

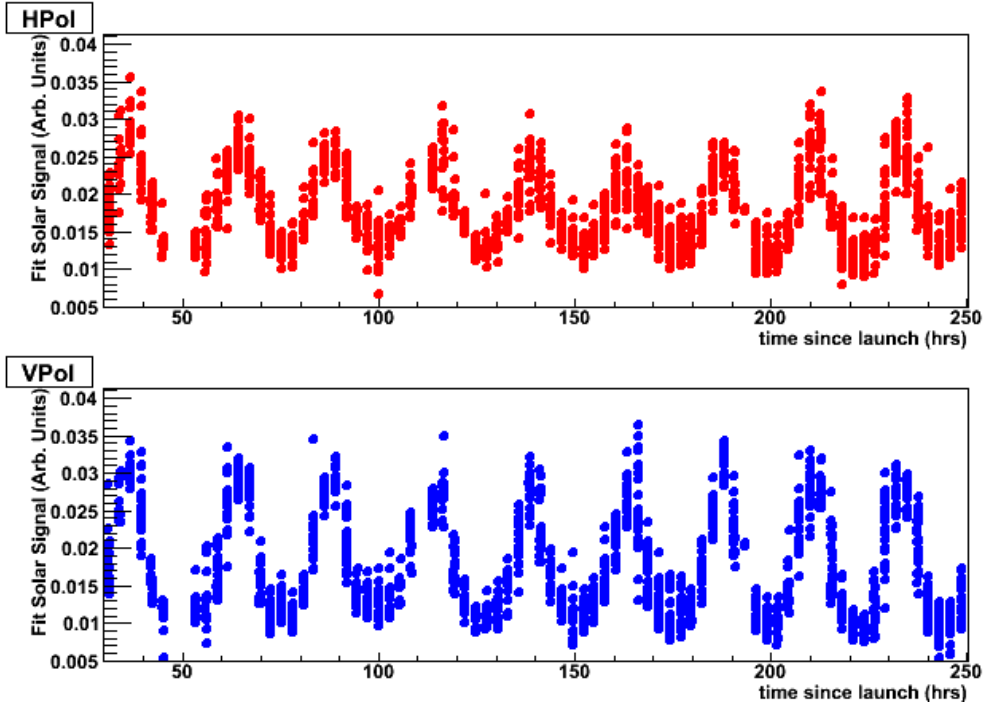


Figure 9: Solar signal strength as a function of number of hours into flight. Normalization is identical for both top and bottom plots.

176 Solar elevation, compared with the expectation from a simple Gaussian parametrization of the Seavey horn beam pattern. We  
 177 observe that the Solar interferometric map can be used, in-flight, to calibrate the off-axis beam pattern to an accuracy of a few  
 178 degrees.

179 **4.1.3. Solar Power as a function of Frequency**

180 Figure 11 shows the absolute spectral power measured at two terrestrial observatories[20, 21], averaged over the time period  
 181 comprised by the ANITA-II mission. Overlaid on that graph is the direct Solar power, as measured interferometrically by ANITA-  
 182 II. We observe reasonable agreement in the shape of the two spectra.

183 **5. Measurement of Surface Radio Reflectivity  $\mathcal{R}$**

184 **5.1. Geometry**

185 As indicated in Figure 2, the typical displacement between the ANITA balloon and the surface reflection point is of order  
 186 hundreds of km. For a sub-sample of data spaced out over the duration of the ANITA-II flight, Fig. 12 shows the latitude and  
 187 longitude of both the gondola and also the ice surface reflection location on the ice surface calculated using the known gondola and  
 188 Solar positions at the time of each event trigger, and taking into account Earth curvature effects. The ANITA flight path samples  
 189 the interior ice sheet, as well as shelf ice and some sea ice at latitudes lower than the Ross Ice Shelf.

190 **5.2. Quantitative Technique**

191 Similar to Figure 8, we can create an enhanced radio frequency reflected Solar image by adding many events. However, whereas  
 192 Figure 8 is obtained by correcting each interferogram, event-by-event, for both the balloon motion as well as the celestial motion  
 193 of the Sun to maintain coherence of the direct Solar image, proper accounting of the reflection requires correcting for balloon  
 194 motion as well as the motion of the Solar reflection point across the ice surface. Although the location of the Solar reflection  
 195 on the surface is obviously closely correlated to the direct Solar motion in azimuth, and also closely anti-correlated to the direct  
 196 Solar motion in elevation, corrections due to local Earth curvature, surface elevation and the viewing angle relative to the surface  
 197 can easily smear the reflection image by an amount exceeding the intrinsic expected Solar beam spot size ( $\sim 1$  degree) and must  
 198 therefore be carefully tracked as the reflection images are stacked. We note that large-scale variations in surface slope gradients in  
 199 Antarctica typically occur over hundreds of km, and constitute, at most, a 0.1 degree smearing for the analysis presented below.

200 For this analysis, to determine the relative reflected:direct observed signal strength, we fit the direct and reflected peaks to  
 201 Gaussian functions, and take the integral under our Gaussian signal parametrization as our primary estimate of the signal power.  
 202 Figures 13 and 14 show the fits to the one-dimensional projections of the reflection-stacked interferometric maps corresponding to  
 203 Fig. 8, from which we extract signal estimates. For simplicity, we have centered the Solar image in the center of the graphs shown.

204 As a cross-check, we have also performed a second, independent analysis, which uses the maximum amplitude pixel in the  
 205 interferometric map, in the vicinity of the known Solar, or reflected location in the sky, as a measure of the signal intensity. This  
 206 technique works well for cases of high signal to noise, which is true for the HPol reflected signal, but becomes decreasingly

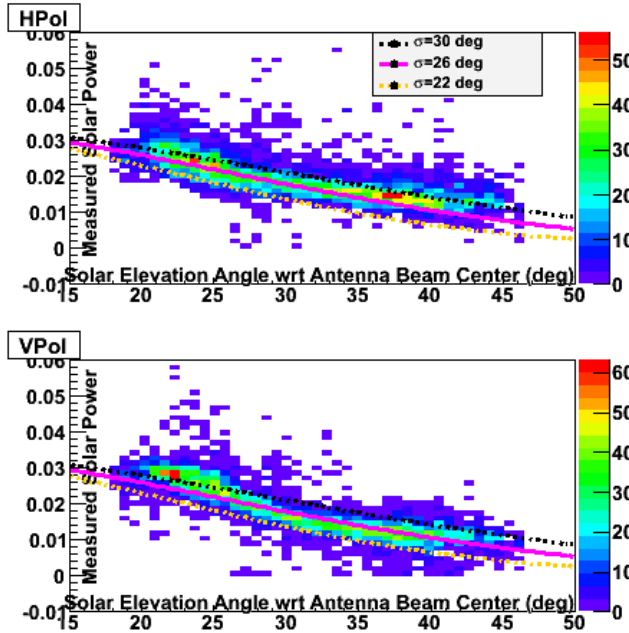


Figure 10: Parametrized antenna gain of varying beam width (lines) compared to relative Solar intensities extracted from Hpol (top) and Vpol (bottom) interferograms. Color scale indicates number of events observed at a given point in graph.

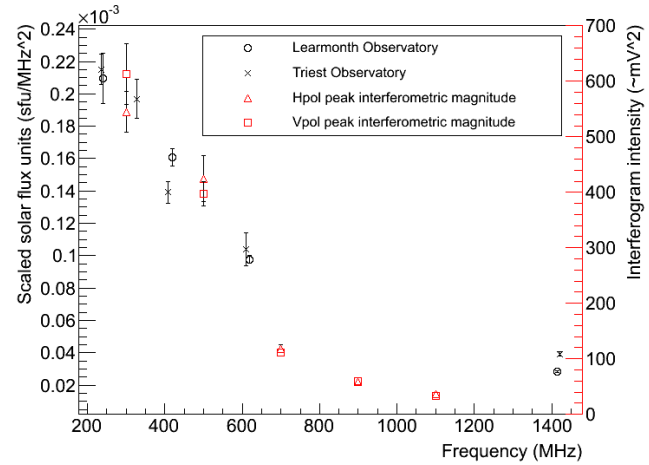


Figure 11: Solar intensities measured at two Solar observatories in Learmonth, Australia (open circles) and Trieste, Italy (crosses) compared to the frequency banded Solar intensities retrieved from the interferograms (Hpol, open triangles and Vpol, open squares). The Trieste data are corrected for latitude of the observations. The ANITA data are obtained from interferograms filtered into five bands (200-400 MHz, 400-600 MHz, 600-800 MHz, 800-1000 MHz, 1000-1200 MHz); points are placed at the center frequency of each band. For each band, we use the same sample of 8000 co-added event triggers. Normalizations have been set to be approximately equal at 200 MHz.

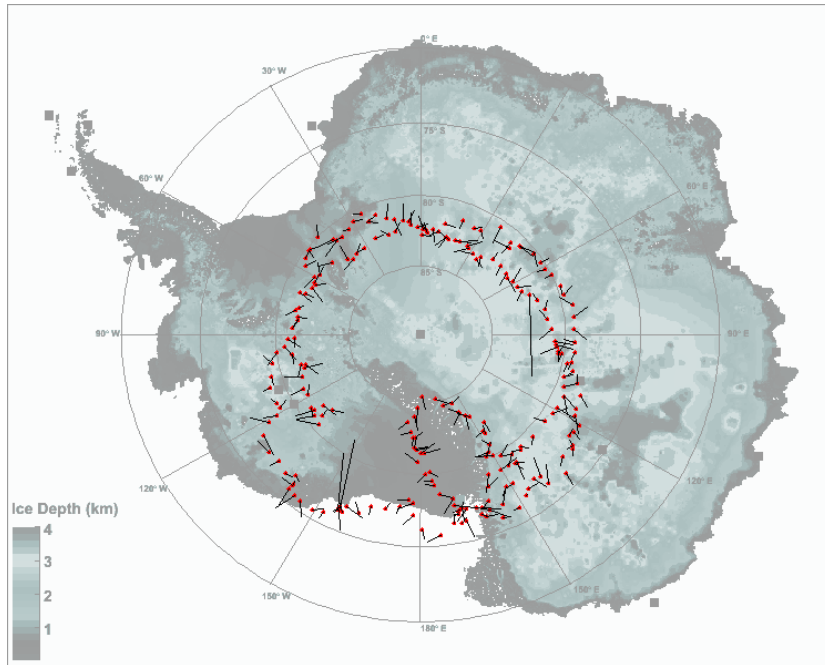


Figure 12: Illustration of typical geometry of ANITA-II gondola relative to surface reflection point. ANITA-II locations sampled during flight are shown for single events. Red points correspond to balloon location; each associated line points to the reflection location on the ice surface.

HPol Fit

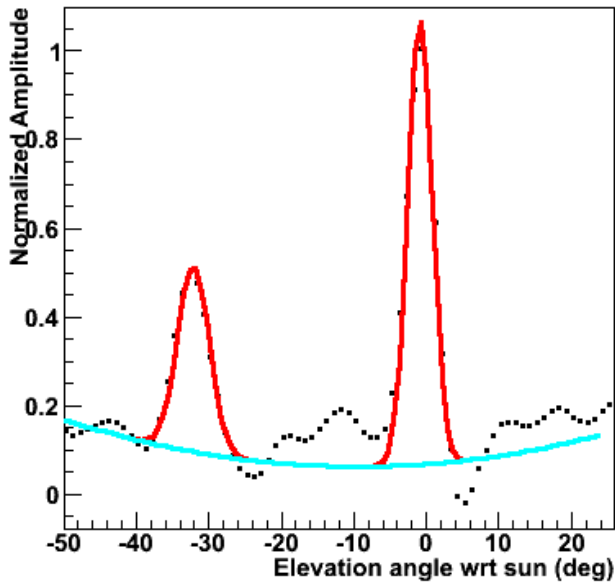


Figure 13: Sample fit to projection of HPol, Sun-centered Solar interferometric map onto elevation axis, after cutting  $\pm 10$  degrees around  $\phi = 0$ . Fit includes two Gaussian-shaped signals, corresponding to direct Solar signal and reflected surface reflection, plus second-order polynomial to approximate non-zero background under Gaussian signals.

VPol Fit

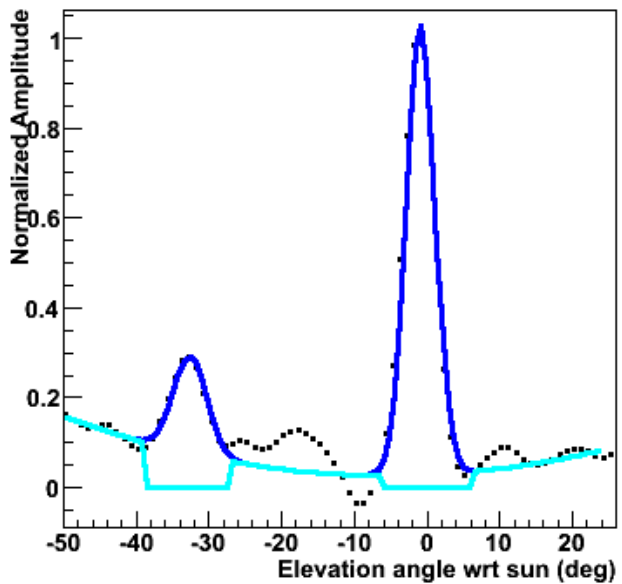


Figure 14: Sample fit of projection of VPol, Sun-centered interferometric map onto elevation axis, after cutting  $\pm 10$  degrees around  $\phi = 0$ . Fit includes two Gaussian-shaped signals, corresponding to direct Solar signal and reflected surface reflection, plus second-order polynomial to approximate non-zero background under Gaussian signals.

207 reliable for low signal-to-noise; correspondingly, we have only applied this cross-check to the HPol case. Fig. 15 displays the  
 208 average ratio  $\mathcal{R}$  of the Solar radio reflection power relative to the direct Solar image, for both vertical as well as horizontal antenna  
 209 polarizations, including all antenna gain corrections, as a function of the reflection angle of the Solar image off the Earth's surface,  
 210 relative to the balloon. Also shown in Fig. 15 are the expected Fresnel reflection power coefficients, assuming specular reflection  
 211 off the Antarctic surface, and taking the index of refraction of the surface snow to be  $n_{surface} = 1.35$ . We note that the gain  
 212 corrections at large incidence angle become quite large for the direct Solar signal, as indicated in Figure 16.

213 We also note that the vertical spread of points relative to the Fresnel expectation in Figure 15 is approximately a factor of three  
 214 larger than the vertical spread of points shown in Figure 10, indicating that the systematic errors for extracting the signal amplitude  
 215 of the weaker surface reflection are considerably larger than the signal estimation uncertainties inherent in the interferometric maps  
 216 themselves.

### 217 5.3. Interpretation

218 Overall, we observe reasonable agreement between the experimental points and the expectation for specular reflection. However,  
 219 we observe an apparent excess, most pronounced for VPol, of the received signal relative to the expectation from the Fresnel  
 220 equations, at higher angles. In particular, we do not observe the predicted signal diminution (approaching zero signal strength)  
 221 at the Brewster angle, which can be attributed to some combination of a) the result of surface roughness effects, which result in  
 222 non-zero signal at the Brewster angle, b) under-accounting of the effects of fringing, c) the asymmetry in the ANITA-II event  
 223 trigger, which tends to favor thermal excursions of VPol over HPol, and d) an under-accounting of the cross-polarization isolation  
 224 between VPol and HPol. Such cross-polarization effects are, in principle, accounted for in Figure 15, but with the assumption  
 225 that the cross-polarization is constant as a function of frequency and off-boresight angle. Our results suggest that isolation may be  
 226 poorer at large off-boresight angles and increasing with frequency.

227 Rigorous simulation of surface effects is beyond the scope of this current work, requiring more extensive data samples on the  
 228 centimeter-scale and shape of the surface features, as well as a cpu-intensive integration across the Antarctic surface. We here  
 229 note only that a simple-minded two-dimensional model comprising an average surface slope of 0.2 radians with a Gaussian power  
 230 spectrum can, at least, reproduce the essential features of our VPol observation, favoring a slight deficit of signal at low incident  
 231 angles relative to the baseline expectation, and an excess at larger incidence angles (Fig. 17).

### 232 5.4. Cross-check: Comparison of reflected intensity over sea ice vs. shelf ice

233 The reflected signal signal strength at an interface depends on the dielectric contrast between the air and the reflecting layer. The  
 234 Solar image reflected off sea ice, having relatively higher salt content, should be brighter than the Solar image reflected off sheet  
 235 ice. As illustrated in Figure 18, we correspondingly note the largest enhancement in the reflected signal strength in the coastal  
 236 region beyond the Ross Ice Shelf, consistent with expectation.

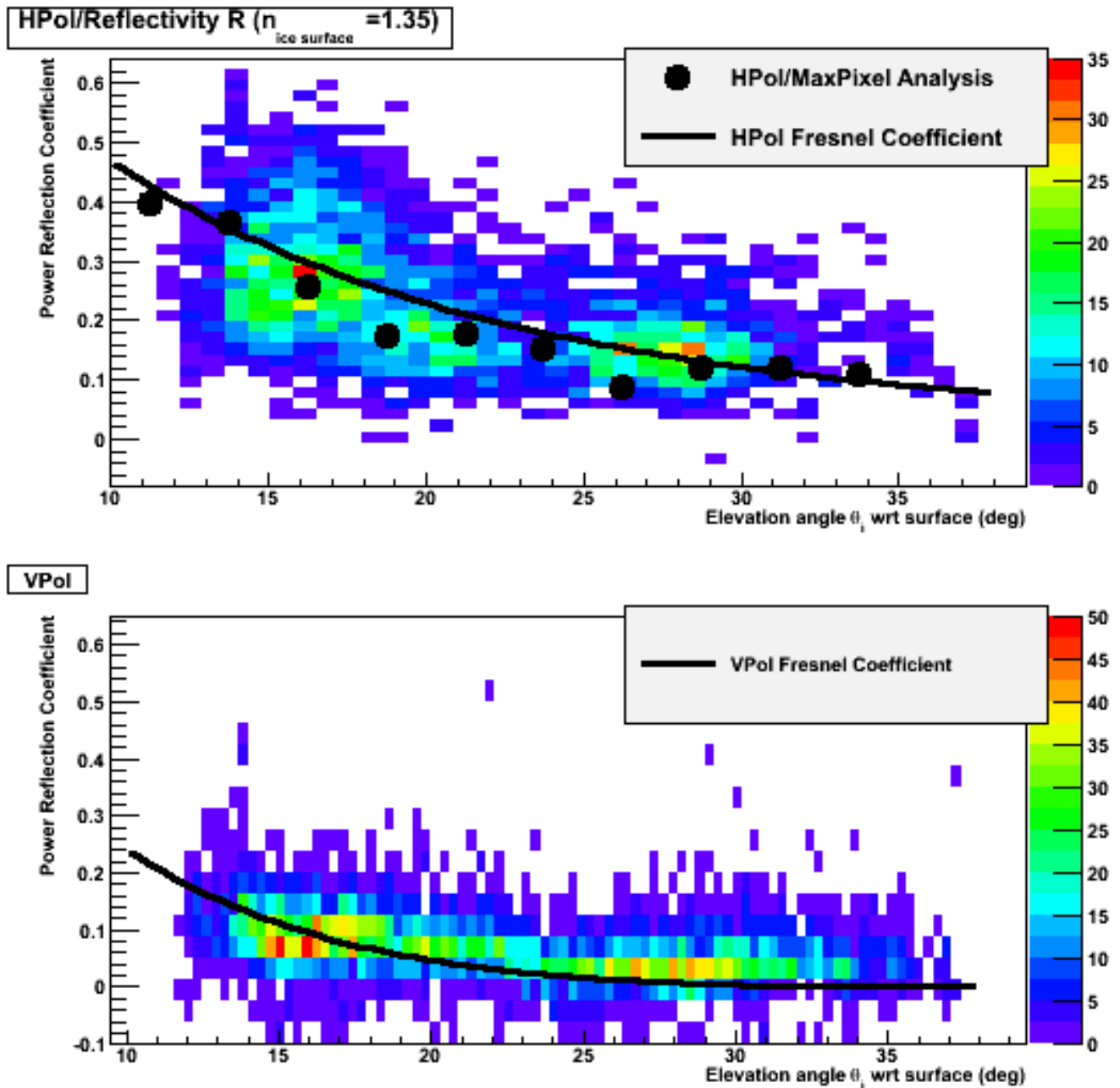


Figure 15: Ratio of ANITA-II measured reflected Solar power to directly-received Solar power, as a function of incident elevation angle, for both HPol and VPol antennas. Overlaid are also calculated values as obtained from direct application of the Fresnel equations to calculate the expected reflected signal power  $\mathcal{R}$ .

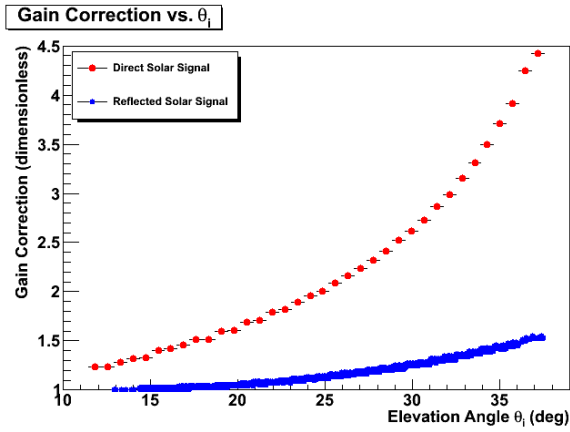


Figure 16: Magnitude of applied gain correction, as function of elevation angle, for direct Solar signal as well as reflection signal.

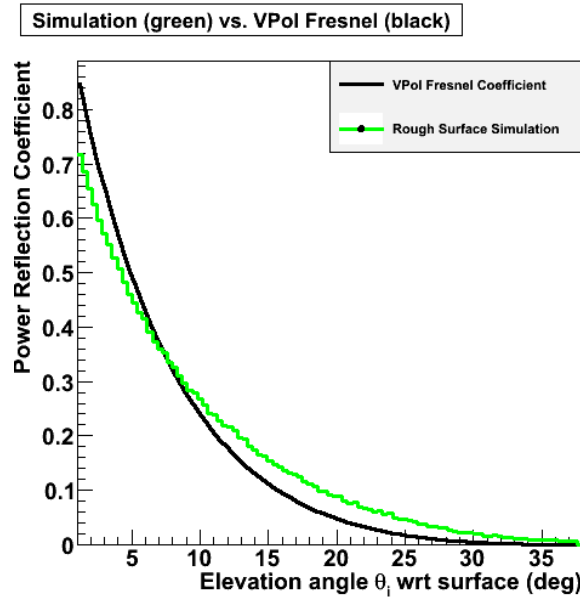


Figure 17: Simulation of expected VPol reflection signal strength using simple model of Gaussian surface of inclination angle 0.2 radians, and with random scattering at all points. Simulation is qualitatively consistent with VPol measurement, showing deficit at low incidence angles and excess at higher incidence angles.

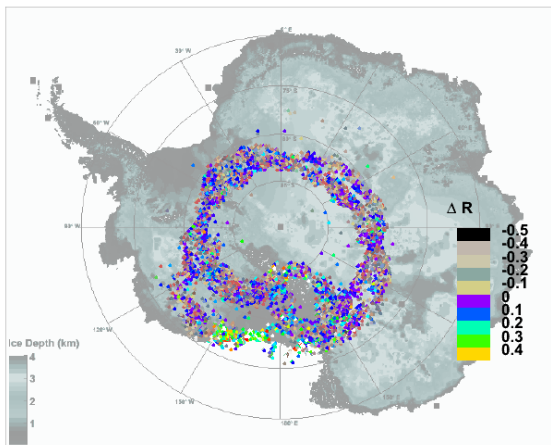


Figure 18: Deviation between measured HPol reflection coefficient relative to reflection coefficient expected at an air-ice sheet interface, as a function of position on the Antarctic continent.

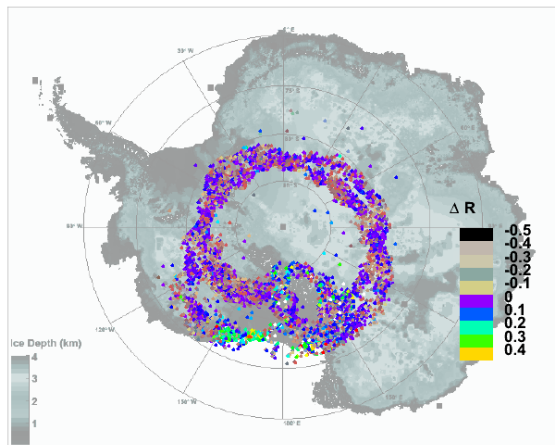


Figure 19: Deviation between measured VPol reflection coefficient relative to reflection coefficient expected at an air-ice sheet interface, as a function of position on the Antarctic continent.

## 237 6. Discussion and Summary

238 To determine the energy of a typical down-coming air shower event, one must estimate the reflectivity of the Antarctic ice  
 239 surface. The reflectivity is, in turn, closely related to the physical scale of surface features, which depend on such parameters as  
 240 local wind speed and direction and surface elevation gradient. Surface roughness also has implications for neutrino detection, as  
 241 high-frequency, small-wavelength radio waves resulting from in-ice neutrino interactions may decohere as they pass through the  
 242 ice-air interface, en route to detection at the ANITA gondola. The wavelength regime to which ANITA is sensitive (125 cm→25  
 243 cm) approaches the expected size of surface inhomogeneities, and therefore underscores the importance of direct surface effect  
 244 measurements.

245 In our current analysis, the ANITA-II balloon-borne radio interferometer has been used to measure the Antarctic surface re-  
 246 flectivity over the ANITA passband. We find reasonable agreement, for both Vertical as well as Horizontally polarized signal  
 247 power, with expectations based on direct application of the Fresnel equations. This analysis therefore provides some basis for  
 248 directly applying the Fresnel coefficients to infer the energies of cosmic rays measured by their surface-reflected radio-frequency  
 249 emissions, as well as the energies of neutrinos detected via their emissions across the air-ice interface. Ongoing analysis will  
 250 incorporate these results, combined with improved simulations of the radio frequency EAS signal, to give revised estimates of the  
 251 observed ANITA-I cosmic ray events. As an indication of what the associated systematic errors in those energy estimates are,  
 252 Figure 20 presents the uncertainty implied by the current analysis. We observe that the typical event-by-event energy uncertainties  
 253 due to surface reflectivity is of order 30-40%, and increasing as the magnitude of the antenna gain correction increases, while the  
 254 deviation between the average reflectivity and expectation, for the large ensemble of events expected for ANITA-3, is typically a  
 255 factor of three smaller.

256 We stress, however, that for the much higher signal-to-noise typical of EAS events, signal energy estimates can be made directly  
 257 from the event waveforms, without relying directly on the interferometric maps to infer signal strength. Variations in the event-by-  
 258 event energy estimate should be considerably smaller than those encountered in the Solar reflection analysis; the systematic errors  
 259 implied by Figure 20 therefore represent a (very) conservative upper limit. As illustration, Figure 21 shows the signal-to-noise  
 260 power ratio measured for higher amplitude calibration pulser events, indicating an intrinsic event-by-event energy uncertainty a  
 261 factor of  $\sim 2$  smaller than what our analysis, based on the lower amplitude Solar signal, might otherwise indicate.

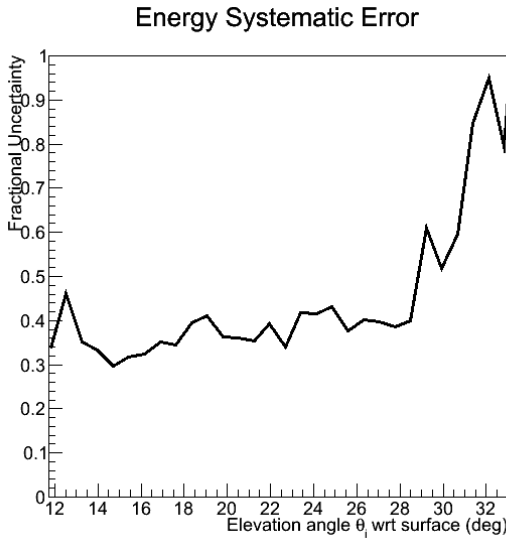


Figure 20: Implied event-by-event radio air shower energy uncertainty, assuming a) errors are equivalent to those obtained in current analysis, and b) energy estimate is dominated by HPol response. Values are dominated by spread in values in Figure 15, rather than observed deviation between measurement and expectation.

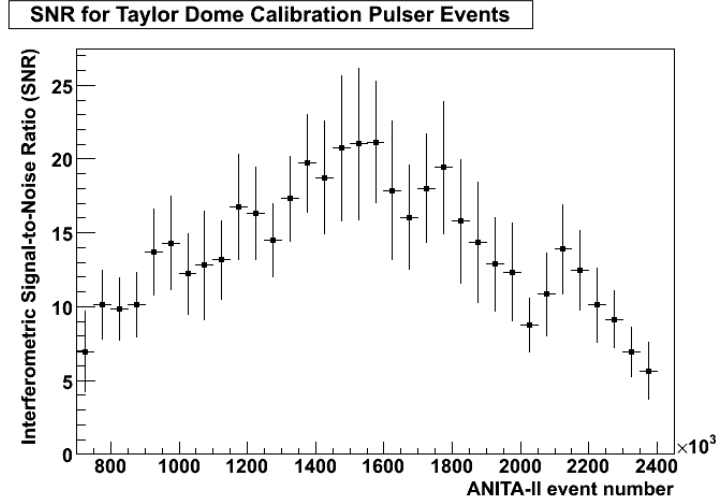


Figure 21: Signal-to-noise ratio measured for calibration pulser events using in-ice transmitter discone at Taylor Dome, as a function of ANITA-II event trigger number. As ANITA-II moves, optimal signal reception occurs approximately at event 1,600,000. Typical scatter within each bin is observed to be of order 20%, taken to be representative of the intrinsic interferometric energy resolution uncertainty for high SNR events.

## 262 7. Acknowledgments

263 We thank the National Aeronautics and Space Administration, the National Science Foundation Office of Polar Programs, the  
 264 Department of Energy Office of Science HEP Division, the UK Science and Technology Facilities Council, the National Science  
 265 Council in Taiwan ROC, and especially the staff of the Columbia Scientific Balloon Facility. A. Romero-Wolf would like to thank  
 266 NASA (NESSF Grant NNX07AO05H) for support for this work.

## 267 References

268 [1] E. Hecht, Optics (4th ed.), Addison Wesley, ISBN 0-321-18878-0, (2002).

269 [2] ANITA Collaboration: P.W. Gorham et al., Astropart. Phys. **32**, 10-41, (2009).  
 270 [3] ANITA Collaboration: D.Z. Besson et al., Astropart. Phys. **29**, 130-157 (2008).  
 271 [4] ANITA Collaboration: P.W. Gorham, et al., Phys. Rev. Lett. **99**, 171101, (2007).  
 272 [5] ANITA Collaboration: P.W. Gorham et al., Phys. Rev. **D82**, 022004 (2010); Phys. Rev. **D85**, 049901(E) (2012).  
 273 [6] C.W. James, et al., Phys. Rev. **D81**, 042003 (2010).  
 274 [7] P.W. Gorham, et al., Phys. Rev. Lett. **93**, 041101 (2004).  
 275 [8] R.L. Mutel, T.R. Jaeger, K.G. Gayley, Nucl. Inst. and Meth. in Phys. Res. **A662**, S24 (2012).  
 276 [9] R. Dagkesamanskii, V. Matveev, and I.M. Zheleznykh, Nucl. Inst. and Meth. in Phys. Res. **A626**, S44, (2011).  
 277 [10] In particular, the HPol trigger was removed and a modification was made to the trigger which effectively required high-frequency signal content, while radio  
 278 air shower events have a sharply falling spectrum over the ANITA bandpass.  
 279 [11] ANITA Collaboration: A. Romero-Wolf et al., “An Interferometric Analysis Method for Radio Impulses from 1 Ultra-high Energy Particle Showers”, in  
 280 preparation (2013).  
 281 [12] ANITA Collaboration: S. Hoover et al., Phys. Rev. Lett. **105**, 151101 (2010).  
 282 [13] K. Greisen, Phys. Rev. Lett. **16**, 748 (1966); G. Zatsepin and V. Kuzmin, Pis'ma Zh. Eksp. Teor. Fiz. **4**, 114 (1966) [JETP. Lett. **4**, 78 (1966)]. V. Berezinsky  
 283 and G. Zatsepin, Phys. Lett. **8B**, 423 (1969); F. W. Stecker, Astrophys. J. **228** 919 (1979).  
 284 [14] Warren, S. G. R. E. Brandt, and P. O'Rawe Hinton, J. Geophys. Res., **103**, 25 (1998).  
 285 [15] X. Wang and C. Zender, J. Geophys. Res., **116**, 16 (2011).  
 286 [16] Parish, T.R., and D.H. Bromwich, Nature, **328**, 51, (1987).  
 287 [17] <http://bprc.osu.edu/rsl/radarsat/data/>  
 288 [18] K. M. Stuart, “Application of SeaWinds Scatterometer Data to the Study of Antarctic Icebergs”, Ph.D. thesis submitted to the faculty of Brigham Young  
 289 University, unpublished (2013).  
 290 [19] F. Remy and Soazig Parouty, Remote Sensing **1**, 1212 (2009).  
 291 [20] [http://www.ips.gov.au/World\\_Data\\_Centre/1/10](http://www.ips.gov.au/World_Data_Centre/1/10)  
 292 [21] <http://radioSun.ts.astro.it/eng/solra.php>